Plasmonics with Two-Dimensional Conductors

Hosang Yoon[1], Kitty Y. M. Yeung[1], Philip Kim[2], Donhee Ham[1]

[1] School of Engineering and Applied Sciences, Harvard University, Cambridge, MA, USA
[2] Department of Physics, Columbia University, New York, NY, USA

Review

Author for correspondence:
Donhee Ham
e-mails: donhee@seas.harvard.edu

A wealth of effort in photonics has been dedicated to the study and engineering of surface plasmonic waves in the skin of three-dimensional bulk metals, due largely to their trait of subwavelength confinement. Plasmonic waves in two-dimensional conductors, such as semiconductor heterojunction and graphene, contrast the surface plasmonic waves on bulk metals, as the former emerge at GHz-THz and infrared frequencies well below the photonics regime and can exhibit far stronger subwavelength confinement. This review elucidates the machinery behind the unique behaviors of the two-dimensional plasmonic waves, and discusses how they can be engineered to create ultra-subwavelength plasmonic circuits and metamaterials for infrared and GHz-THz integrated electronics.

1. Introduction

Surface plasmons propagating in the skin of a bulk—three-dimensional (3D)—metal with a finite penetration depth have nucleated a great deal of research in photonics, because they can travel up to ~10 times slower than the free-space light (speed c), and thus can exhibit subwavelength confinement with proportionally reduced wavelength [1-4]. In contrast to these surface plasmons on bulk metals that emerge in the optical frequencies, the plasmons in GaAs/AlGaAs two-dimensional (2D) electron gas (2DEG) and graphene, where electrons are perfectly confined into two dimensions, appear at infrared and THz-GHz frequencies, near or in the electronics regime. Furthermore, the 2D plasmons can achieve much greater subwavelength confinement [5-7] with their velocity being able to reach well below $c/100$ [6,8].

By shaping the 2D conductor geometry with the standard fabrication technology and manipulating 2D plasmonic waves via reflection, interference, and coupling according to the geometry, a variety of ultra-subwavelength 2D plasmonic circuits and metamaterials, such as

bandgap crystals, interferometers, resonant cavities, and negative refractive index structures, can be created [6,8,9] for GHz-THz and infrared integrated electronics with applications in imaging, large molecule spectroscopy, and sub-millimeter wave astronomy. The ultra-subwavelength confinement of these 2D plasmonic structures suggests exciting possibilities for sub-diffraction-limit imaging, near-field operation, and drastic miniaturization.

This review paper will first elucidate the unique behavioral characteristics of plasmonic waves in 2D conducting media and their physical origin (Section 2). Then we will delineate how 2D plasmonic waves can be engineered to build functional circuits and metamaterials, using some recent device advances as examples (Section 3).

2. Physical Characteristics of 2D Plasmonic Waves

Perturbation of the equilibrium electron density distribution in a solid-state conductor—whether 3D or 2D—results in Coulomb restoring force, which drives local electrons back and forth collectively to propel a plasmonic wave. The defining energetic component of a plasmonic wave is the kinetic energy of the collectively oscillating electrons, which largely accounts for the plasmons' behavioral difference from light waves, in particular, the reduced plasmonic velocity and subwavelength confinement. The kinetic energy is far more strongly pronounced in 2D plasmonic waves than in 3D bulk metal surface plasmonic waves [6,9]. Consequently, the behavior of 2D plasmons diverges even more significantly from light waves than that of 3D surface plasmons does; for example, and notably, 2D plasmons can achieve a significantly lower velocity thus a much greater subwavelength confinement than 3D surface plasmons. This section explicates the origin of the unique behaviors of 2D plasmonic waves in comparison to 3D bulk metal surface plasmonic waves.

(a) Transmission Line Model for 2D Plasmonic Medium

As will be discussed shortly, the kinetic energy of the collectively oscillating electrons in a 2D plasmonic wave can be modeled using *kinetic* inductance of non-magnetic origin [6,9]. On the other hand, the electric potential energy associated with the Coulomb restoring force that drives local electrons into the plasmonic oscillation can be modeled using electrical capacitance. Besides the Coulomb restoring force, electron degeneracy pressure serves as another restoring mechanism upon the disturbance of the equilibrium electron density distribution, and this effect can be modeled using quantum capacitance [5,10-12]. This quantum pressure, however, becomes conspicuous only when the Coulomb restoring force is substantially weakened by, for example, placing a gate very proximate to the 2D plasmonic medium and reducing the Coulomb interaction range; throughout this paper, we will ignore the quantum effect. Then the 2D plasmonic medium can be modeled as a transmission line consisting of distributed kinetic inductance L_k per unit length and distributed electrical capacitance C per unit length (Fig. 1) [6,9,13]. This plasmonic transmission line differs from the standard electromagnetic transmission

line in that the latter employs magnetic inductance instead of kinetic inductance. The plasmonic velocity is then $v_p = 1/(L_k C)^{1/2}$, which corresponds to the plasmonic dispersion relation.
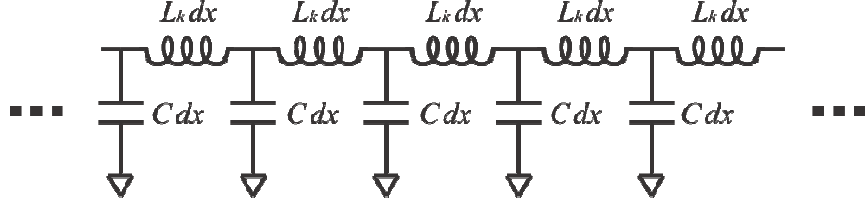

Figure 1. Transmission line model of a 2D plasmonic medium. If the medium is gated, the gate serves as the ground. For an ungated medium, the ground is the potential of the free space far enough away. dx: infinitesimal segment length of the 2D plasmonic medium.

We first evaluate L_k in the 2D conductor case where electrons have finite effective mass, m^*, such as in GaAs/AlGaAs 2DEG (width W and length l) [9]. Let a time-dependent electric potential $V(t)$ be applied along the length to induce an electric field $V(t)/l$. Here the length l is chosen so short that the electric field does not exhibit a spatial variation; this is not a limiting assumption, as the goal is to derive the kinetic inductance per unit length. Inertial accelerations occur, for which Newton's equation of motion for an electron is $-e(V/l) = m^*(dv/dt)$ (v: electron velocity). This translates to $-e(V/l) = i\omega m^* v$ in the frequency domain. From this and by noting that the current due to the electrons' motion is $I = -n_{2D}evW$ (n_{2D}: conduction electron density per unit area), the 2D conductor's impedance is obtained: $V/I = i\omega \times (m^*/n_{2D}e^2)(l/W)$. This is inductive impedance of non-magnetic origin, with the kinetic inductance per unit length given by

$$L_k = (m^*/n_{2D}e^2) \times (1/W). \tag{2.1}$$

By using $k_F^2 = 2\pi n_{2D}$ and $E_F = \hbar^2 k_F^2/(2m^*)$ (k_F: Fermi wavenumber, E_F: Fermi energy), we can rewrite Eq. (2.1) as:

$$L_k = (\pi\hbar^2/e^2) \times (1/E_F) \times (1/W). \tag{2.2}$$

The kinetic energy of the accelerating electrons is intimately linked to the kinetic inductance. With the velocity v of an electron at a given time, the total kinetic energy K_{total} of the electrons in the 2D conductor strip is expressed $K_{total} = m^* v^2/2 \times n_{2D}Wl$. Since the total current is $I = -n_{2D}evW$, we can write

$$K_{total} = 1/2 \times (L_k l) \times I^2, \tag{2.3}$$

where $L_k l$ is the total kinetic inductance of the 2D conductor strip. Eq. (2.3) is analogous to the energy of a magnetic inductor with current I given by $1/2 \times$ (magnetic inductance) $\times I^2$.
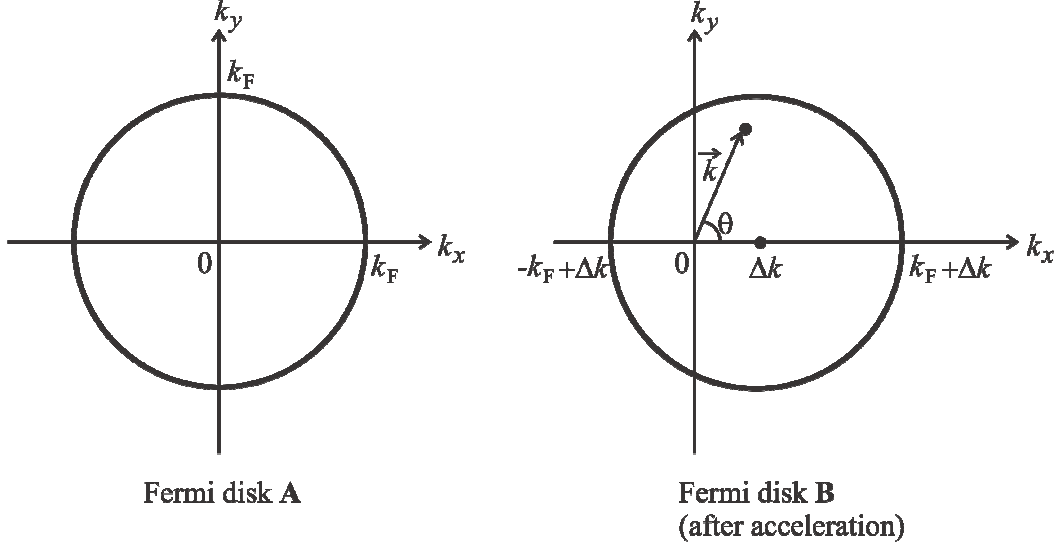

Figure 2. Shift of the Fermi disk in the k-space in response to an electric field.

Alternatively, we can instead calculate L_k by first evaluating the total kinetic energy K_{total} and current I in the k-space (k: electron wavenumber) and then relating them through the energy-current relation, Eq. (2.3) [9]. With the electric field applied along the length of the 2D conductor strip to which direction we assign a negative x-axis, the 2D Fermi disk with diameter k_F whose center originally lies at the k-space origin (Fig. 2, **A**) shifts towards the positive k_x-axis, increasing the total kinetic energy and producing a current I. Figure 2, **B** shows the Fermi disk shift by $\Delta k << k_F$, after time Δt. The total kinetic energy increase is:

$$K_{total} = Wl \iint_B 2\frac{dk_x}{2\pi}\frac{dk_y}{2\pi}E(\vec{k}) - Wl \iint_A 2\frac{dk_x}{2\pi}\frac{dk_y}{2\pi}E(\vec{k}), \qquad (2.4)$$

where the factor 2 in each integrand accounts for spin degeneracy and $E(\vec{k}) = \hbar^2 k^2/(2m^*)$ is the energy of a single electron whose wavenumber is k. Keeping to the lowest order of Δk, it is a straightforward exercise to show that Eq. (2.4) leads to

$$K_{total} = \frac{WlE_F}{2\pi} \times (\Delta k)^2. \qquad (2.5)$$

On the other hand, the current magnitude I is given by:

$$I = W \iint_B 2\frac{dk_x}{2\pi}\frac{dk_y}{2\pi}ev_x(\vec{k}), \qquad (2.6)$$

4

where $v_x(\vec{k})$ is the *x*-component of the velocity of an electron whose wave vector is $\vec{k}$, that is, $v_x(\vec{k}) = (\hbar k/m^*)\cos\theta$, where the integration variable θ is in reference to Fig. 2. Keeping to the lowest order of Δk, one can show that Eq. (2.6) reduces to

$$I = \frac{WeE_F}{\pi\hbar}\times\Delta k.$$ (2.7)

Eqs. (2.5) and (2.7) satisfy the energy-current relation of Eq. (2.3) with L_k given by:

$$L_k = (\pi\hbar^2/e^2) \times (1/E_F) \times (1/W),$$ (2.8)

which is identical to the L_k-expression of Eq. (2.2).

The second approach to calculate L_k is more general than the first approach, because the second approach can be applied to any arbitrary single electron *E-k* dispersion. In particular, in the linear *E-k* dispersion case of graphene—another example of 2D conductor—where individual electrons behave as massless particles [14,15], the first approach cannot be used but the calculation in the second approach can be repeated now with $E(\vec{k}) = \hbar v_F k$, $v_x(\vec{k}) = v_F\cos\theta$, and with the appropriate degeneracy factor including both spin and valley degeneracies (v_F: Fermi velocity) [16,17]. The application of the second approach to the calculation of the graphene kinetic inductance turns out to be identical to Eq. (2.8).

The per-unit-length capacitance, *C*, in the 2D plasmonic transmission line [Fig. 1], which models the Coulomb restoring force in the plasmonic wave, depends on surroundings of the plasmonic medium. For example, if a 2D conductor strip with width *W* has no other conductors nearby, *C* for a given plasmonic wavenumber k_p is given by [18,19]

$$C = 2\varepsilon k_p W,$$ (2.9)

where ε is the electric permittivity of the surroundings. This is obtained by calculating the electric energy of the sinusoidal charge density distribution at a plasmonic wavenumber, k_p.

As the plasmonic velocity is $v_p = \omega/k_p = 1/(L_k C)^{1/2}$, we can now obtain the detailed expression for the 2D plasmonic dispersion. In the case of the stand-alone 2D conductor where *C* is given by Eq. (2.9), by using L_k of Eq. (2.8), whether the 2D conductor is semiconductor 2DEG or graphene, we obtain:

$$\omega = \frac{k_p}{\sqrt{L_k C}} = \sqrt{\frac{e^2 E_F}{2\varepsilon\pi\hbar^2}k_p}\ .$$ (2.10)

Calculation in the random phase approximation framework yields a more general form of the 2D plasmonic dispersion relation [5,20], but in the limit where quantum effects such as electron

degeneracy pressure and interband transitions can be ignored, the general dispersion reduces to Eq. (2.10) for both semiconductor 2DEG and graphene [5,21].

If an external conductor is proximate to the 2D conductor, C is altered. A case of particular interest is a gated 2D conductor. If the separation, d, between the gate and 2D conductor is much smaller than the plasmonic wavelength ($k_p d \ll 1$), C becomes the parallel plate capacitance per unit length, $C = \varepsilon W/d$. The 2D plasmonic dispersion then becomes linear for both semiconductor 2DEG and graphene [11,22]:

$$\omega = \frac{k_p}{\sqrt{L_k C}} = k_p \sqrt{\frac{e^2 E_F d}{\varepsilon \pi \hbar^2}} \, . \tag{2.11}$$

As compared to the stand-alone 2D conductor, the gated configuration yields smaller plasmonic wavelength and velocity [Eqs. (2.10) vs. (2.11)]. This is because the gate shortens the Coulomb interaction range. For the same reason, as d is shortened, the plasmonic velocity and wavelength are further reduced. These 2D plasmonic dispersions for stand-alone or gated cases have been experimentally demonstrated for both semiconductor 2DEG [6,8] and more recently for graphene [7,23,24].

(b) 2D Plasmons v. 3D Surface Plasmons

While we have focused on the transmission line model for the 2D plasmonic medium, a similar transmission line model consisting of kinetic inductance and electrical capacitance can be used to model the surface plasmonic medium in the skin of the 3D bulk metal with the finite penetration depth, for the two main energetic components of the surface plasmonic wave on the 3D metal are also the kinetic energy of collectively oscillating electrons and the electric potential energy corresponding to the Coulomb restoring force [19]. In contrast, light waves possess magnetic and electric energies as two energetic components. By comparison one can see that the kinetic energy of plasmonic waves (whether 2D plasmons or 3D surface plasmons) is responsible for their behavioral divergence from light waves.

To describe the behavioral difference between 2D plasmonic waves and 3D metal surface plasmonic waves, we now evaluate the kinetic inductance associated with the 3D surface plasmonic wave. The collective oscillation of electrons in 3D surface plasmonic waves occurs within the skin of a bulk conductor, whose frequency-dependent penetration depth, δ, decreases with increasing frequency. The per-unit-length kinetic inductance of this skin with width W can be derived by considering inertial acceleration of electrons therein, as in the first approach given in the previous subsection (for 3D conductors, there is no particular reason to consider massless electrons):

$$L_{k,skin} = (m^*/n_{3D}e^2) \times (1/W\delta), \tag{2.12}$$

where n_{3D} is conduction electron density per unit volume. Using $k_F^3 = 3\pi^2 n_{3D}$ and $E_F = \hbar^2 k_F^2/(2m^*)$, we can rewrite Eq. (2.12) into

$$L_{k,skin} = (3\pi^2\hbar^2/2e^2) \times (1/E_F) \times (1/W) \times (1/k_F\delta). \tag{2.13}$$

Eqs. (2.13) and (2.8) show that kinetic inductance in either 3D or 2D case increases as the total number of electrons is reduced. This can be understood as follows. When there are fewer electrons, they need to accelerate to a proportionally higher velocity to produce the same current. The total kinetic energy then becomes larger, as it is proportional to the number of electrons but to the *square* of the electron velocity. Since we have fixed the current, the kinetic inductance then should be larger, according to Eq. (2.3).

When 2D kinetic inductance L_k of Eq. (2.8) and 3D kinetic inductance $L_{k,skin}$ of Eq. (2.13) are juxtaposed, the $1/(k_F\delta)$ factor in $L_{k,skin}$ makes an apparent difference. Since the penetration depth δ decreases with frequency in the 3D surface plasmonic dynamics, $L_{k,skin}$ increases with frequency; this is essentially because the reduced δ decreases the number of conduction electrons participating in the surface plasmonic wave. At frequencies below the optics regime, δ is large enough to render $L_{k,skin}$ unappreciable as compared to the magnetic inductance of the surface plasmonic medium. Hence, it is difficult to observe surface plasmons below the optics regime with 3D metals, and 3D surface plasmonic dispersion curve deviates away from the light dispersion line only towards the optics regime (Fig. 3). By contrast, L_k of the 2D plasmonic medium has no frequency dependency, as there is no such frequency-dependent penetration depth where electrons are confined perfectly into two dimensions. Moreover, L_k is orders of magnitude larger than the magnetic inductance of the 2D conductor. Therefore, the 2D plasmonic wave emerges far below the optics regime, with its dispersion curve deviating significantly away from the light line at these low frequencies (Fig. 3).
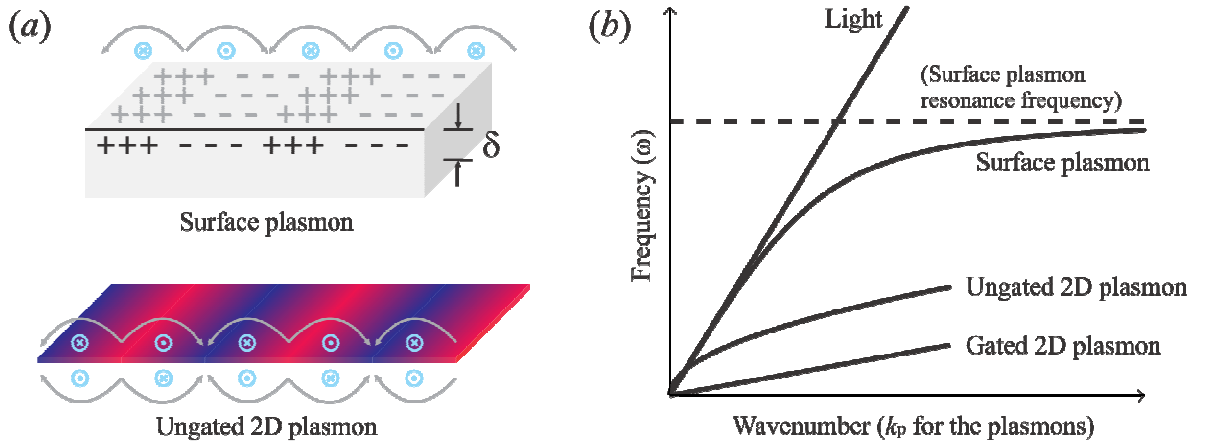

Figure 3. (a) Illustration of the charge, electric field (gray arrows), and magnetic field (blue arrows) associated with surface plasmonic wave on 3D bulk metal and with 2D plasmonic wave in an ungated 2D conductor. (b) Essence-capturing hypothetical dispersion curves for light wave, 3D surface plasmonic wave, ungated 2D plasmonic wave, and gated 2D plasmonic wave.

Even when $L_{k,skin}$ becomes appreciable in the optics regime with small enough δ and surface plasmonic dynamics is more pronounced, $k_F\delta$ is still much larger than 1, leaving $L_{k,skin}$ $<< L_k$ (in principle $L_{k,skin}$ can grow indefinitely as frequency grows toward the surface plasmon resonance frequency with δ approaching 0, but in practice loss obscures such excitations). The $L_{k,skin} << L_k$ inequality is further enhanced by the fact that E_F appearing in both $L_{k,skin}$ and L_k is typically much larger with the 3D bulk metal such as gold than with semiconductor 2DEG and graphene. Overall, $L_{k,skin}$ even in the optics regime is far smaller than L_k by 2 ~ 3 orders of magnitude. As $v_p \propto$ [kinetic inductance]$^{-1/2}$, 2D plasmonic velocity is far smaller than 3D surface plasmonic velocity typically limited to ~ c/10 [1] (Fig. 3), achieving far greater ultra-subwavelength confinement. One can further slow the 2D plasmonic wave by placing a gate proximate to the 2D conductor and thus by shortening the Coulomb interaction range within the 2D conductor (*i.e.*, by increasing C; note that $v_p = 1/(L_kC)^{1/2}$) [Eq. (2.10) v. Eq. (2.11); Fig. 3]; in fact, with top-gated GaAs 2DEG, we were able to obtain 2D plasmonic velocities as low as ~ c/700 [6].

(c) Effect of Electron Scattering

Electron scatterings with phonons and lattice impurities in the 2D plasmonic medium are manifested as per-unit-length ohmic resistance R, which can be added to the transmission line model of Fig. 1 in series with L_k. The quality factor of the 2D plasmonic medium is then given by

$$Q = \omega L_k/R = \omega\tau, \tag{2.14}$$

where the electron scattering time τ factors in through R (note that we here are not considering loss mechanism due to interband transitions, for in practice many plasmonic applications can be considered at frequencies where such transitions do not occur). The plasmonic dynamics can be observed as far as Q is not too far below 1, *i.e.*, if τ is long enough to accommodate an appreciable kinetic energy increase (if Q is much larger than 1, many cycles of collective electron oscillation are sustained between scattering events, making the plasmonic wave very easily observable). To observe 2D plasmonic waves at GHz frequencies, τ has to be increased, which can be done by cryogenic operation, as applicable for GaAs/AlGaAs 2DEG where τ is limited by phonon scattering down to substantially lowered temperature, but not as well with graphene where impurity scattering is significant even at room temperature. At THz and infrared frequencies, room temperature plasmonic operation is possible with both semiconductor 2DEG and graphene, as experimentally demonstrated [7,25].

3. Applications – Ultra-Subwavelength 2D Plasmonic Circuits and Metamaterials

A 2D plasmonic medium can be readily shaped into a designer planar geometry by using the standard fabrication technology. 2D plasmonic waves then can be manipulated by reflections, interferences, and superposition according to the geometry. In this way, one can create a variety

of GHz-THz and infrared 2D plasmonic circuits and metamaterials [6,8,9]. Due to their ultra-subwavelength confinement, these 2D plasmonic functional structures are amenable to near-field operation, sub-diffraction-limit imaging, and drastic miniaturization.
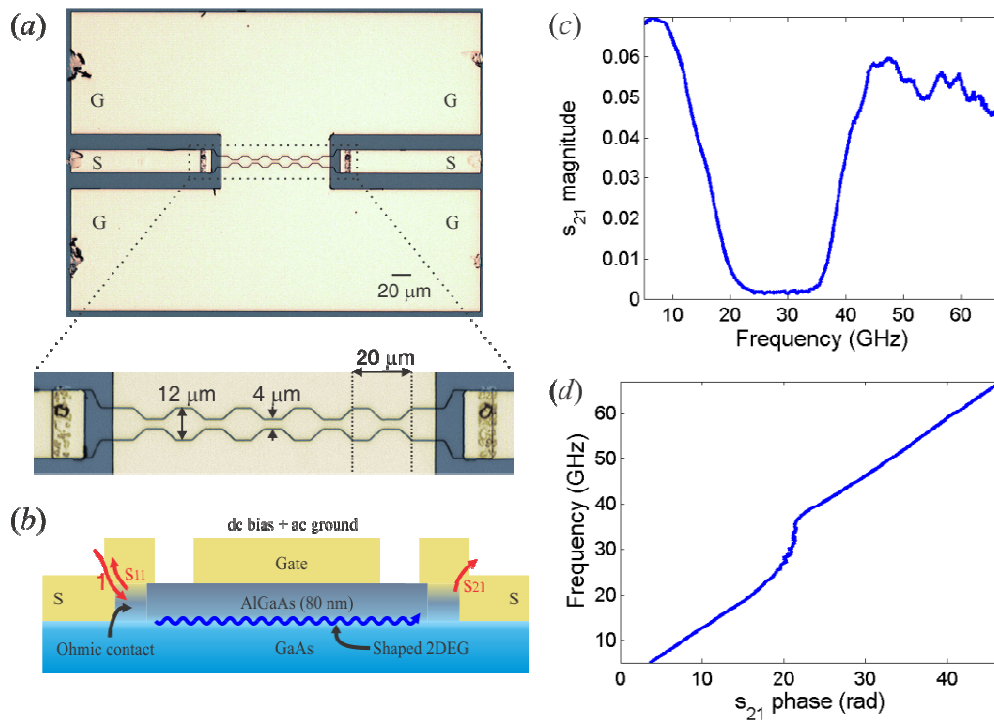

Figure 4. (a) 2D plasmonic crystal with GaAs/AlGaAs 2DEG. (b) Cross-sectional schematic. (c,d) Measured s_{21} magnitude and phase. Reprinted with permission from *Nano Lett*. **12**, 2272 (2012). Copyright © 2012 American Chemical Society.

An example of 2D plasmonic circuits is plasmonic bandgap crystals, which can be created by introducing structural periodicity into a 2D conductor. These plasmonic bandgap crystals are analogous to photonic bandgap crystals [26,27], but the former operate far below the optical frequencies and exhibit much greater subwavelength confinement. A proof-of-concept 2D plasmonic crystal, which W. F. Andress *et al* built from GaAs/AlGaAs 2DEG and operates in the GHz frequencies at cryogenic temperature (4.2K), is shown in Fig. 4 [6]. The 2DEG was periodically shaped by spatially modulating its width (Fig. 4a), and was placed between electromagnetic metallic coplanar waveguides (CPWs), consisting of signal (S) & ground (G) lines, where the S lines couple to the 2DEG via ohmic contacts (Figs. 4a-b). The 2DEG is placed under a metallic gate, which is merged with the CPWs' G lines; in this way, the top gate not only enhances the subwavelength confinement of 2D plasmonic waves, but serves as the proper plasmonic ground. Due to the crystal periodicity, the magnitude of the transmission parameter s_{21} obtained from microwave scattering measurements shows a bandgap (24~34 GHz) around the first Brillouin-zone boundary (Fig. 4c), where the crystal periodicity equals half the plasmonic

wavelength, indicating $v_p \sim c/300$. The phase of the measured s_{21} is a product of plasmonic wavenumber k_p and the crystal length, thus, s_{21}'s phase over the frequency (Fig. 4d) yields the dispersion, which also shows the bandgap behavior. Its passband slope, which is linear due to the gating [Eq. (2.11)], consistently indicates $v_p \sim c/300$.
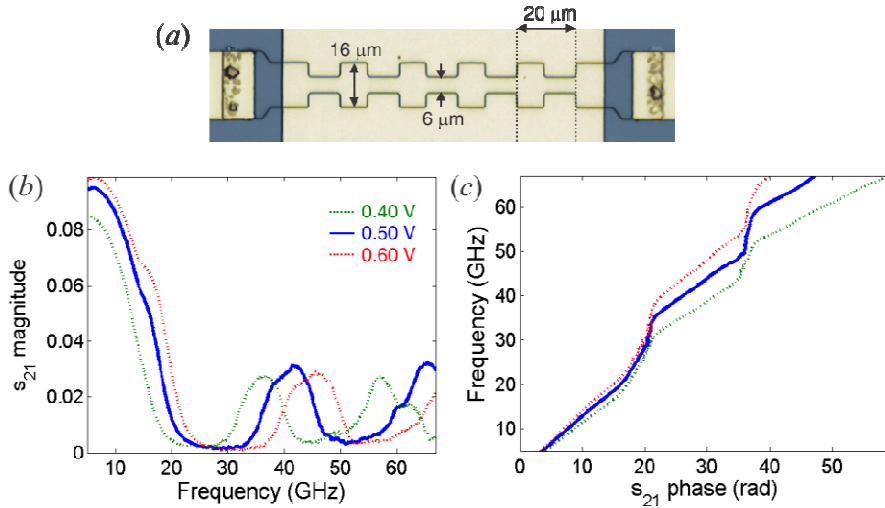

Figure 5. (a) Another linear 2D plasmonic crystal with GaAs/AlGaAs 2DEG. (b,c) Measured s_{21} magnitude and phase. Reprinted with permission from *Nano Lett.* **12**, 2272 (2012). Copyright © 2012 American Chemical Society.

The shaping principle can be applied with a wealth of versatility. For instance, one can subtly vary the crystal shape to introduce an appreciable behavioral difference. Fig. 5a shows an example variation [6], where the transitions between narrow and wide 2DEG sections are abrupt. Plasmonic dynamics here is not a merely disturbed horizontal routing as in Fig. 4. Vertical routing of plasmons to and from the ends of the thick sections (stubs) must be considered; in fact, these stubs serve as plasmonic cavities that resonate by forming a $\lambda_p/4$ standing wave (or its harmonics at higher frequencies), a superposition of plasmonic waves traveling to and reflected from the stub ends. Thus, the repetition of the stubs results in an extra bandgap (~52 GHz) arising from the $\lambda_p/4$ standing wave resonance, in addition to the Brillouin-zone-boundary bandgap (Fig. 5b-c). By further exploiting the versatility of 2D medium shaping, W. F. Andress *et al* also created plasmonic crystals with two-directional periodicity by etching periodic lattices of holes into 2DEG (Fig. 6a). For 2D plasmons traveling horizontally, a bandgap occurs around the first Brillouin-zone-boundary, at which the separation between two adjacent vertical crystal planes equals $\lambda_p/2$. Indeed, two rectangular lattices and a hexagonal lattice made out of 2DEG in Fig. 6a produce expected bandgaps measurements (Fig. 6b).

Another exciting avenue to explore is to create plasmonic interferometers. We recently demonstrated a two-path interferometer of Mach-Zehnder type where two 2D plasmonic waves

undergoing different phase delays are made to interfere [8]. These on-chip 2D plasmonic interferometers exhibit a higher sensitivity to the effective path length difference as compared to
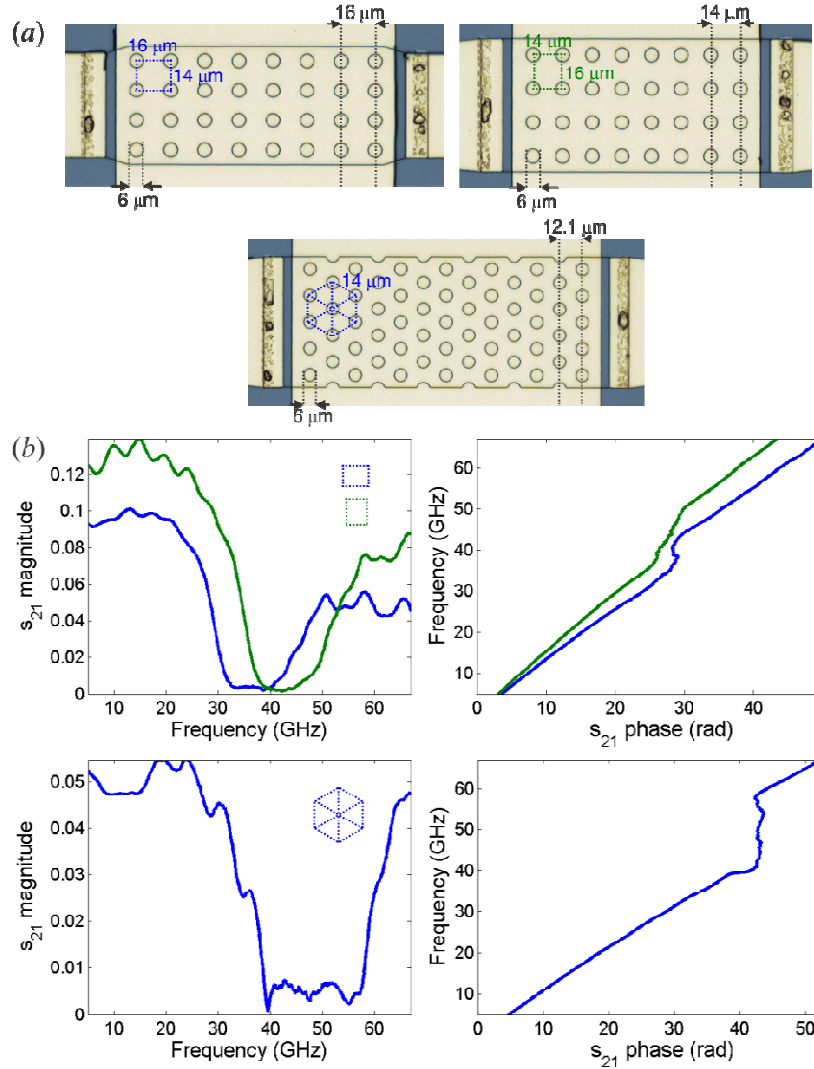

Figure 6. (a) Rectangular and hexagonal 2D plasmonic crystals (GaAs/AlGaAs 2DEG). (b) Measured s_{21} magnitude (left) and s21 phase (right) of rectangular (top) and hexagonal (bottom) crystals. Reprinted with permission from *Nano Lett.* **12**, 2272 (2012). Copyright © 2012 American Chemical Society.

interferometers employing electromagnetic waves, due to 2D plasmons' ultra-subwavelength confinement. The 2D plasmonic interferometers may thus be useful for highly precise and sensitive signal detection, modulation and demodulation, and biomolecular and chemical sensing, in particular, at THz and infrared frequencies.

Negative index metamaterials have been a topic of interest due to their unusual abilities that can lead to technologically gainful applications, and a broad array of negative index metamaterials have been synthesized by engineering electric, magnetic, or optical properties of materials [28-32]. Ultra-subwavelength 2D plasmons, in particular, their associated large 2D kinetic inductance, can be engineered by shaping the 2D conductor geometry to create a new type of metamaterials with extraordinarily strong negative refraction. Using kinetic inductance for negative refraction was envisioned with 3D metallic nanoparticles [33] and experimentally glimpsed with 3D metal surface plasmons [34], but 3D kinetic inductance is far smaller than 2D kinetic inductance, and the two works yielded negative indices less than -5. In contrast, we recently obtained a negative index as large as -700 by exploiting the large 2D kinetic inductance [9]. The large negative index, which corresponds to ultra-subwavelength confinement of negatively refracting wave, can bring the science of negative refraction into drastically miniaturized scale and enable sub-diffraction-limit imaging.
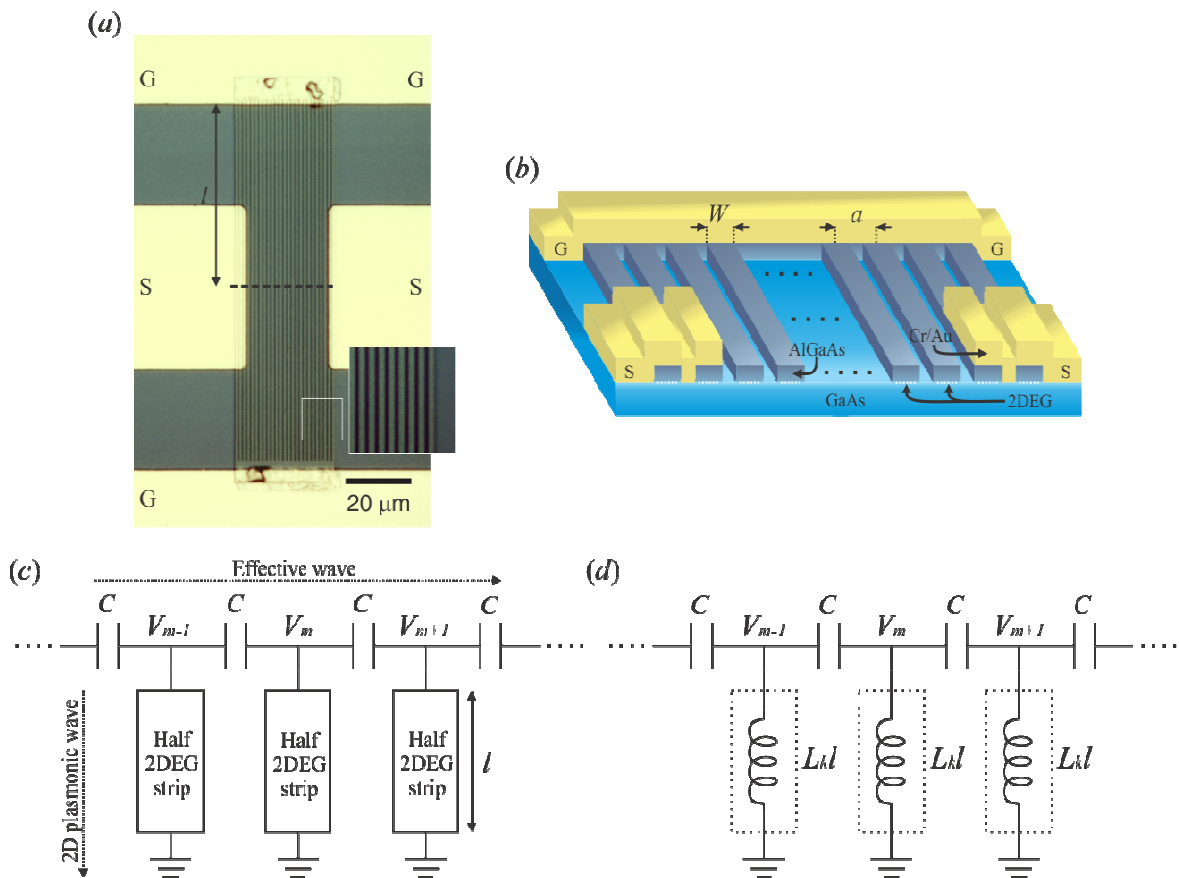

Figure 7. (a) 2DEG strip array. (b) Schematic with the front face cut at the dashed line of part (a). (c) Half-circuit model for the metamaterial. (d) The half 2DEG strip in part (c), which is a 2D plasmonic medium, may be modeled as a lumped kinetic inductor, if the plasmonic wavelength is much longer than the half 2DEG strip. Reprinted with permission from *Nature* **488**, 65 (2012). Copyright © 2012 Nature Publishing Group.

Figure 7 shows a proof-of-concept negative index metamaterial operating at GHz frequencies and cryogenic temperature (up to 20 K) from the aforementioned work of ours [9]. It is an array of ungated GaAs/AlGaAs 2DEG strips (Figs. 7a-b). Metallic CPWs consisting of signal lines (S) flanked by ground lines (G) are used to guide signals to and from the device. Each 2DEG strip is tied to the G lines at its both ends via ohmic contacts. The left S line extends up to over a few strips on the left side. The excitation electromagnetic wave's electric fields between the signal and ground lines of the left CPW excites 2D plasmonic waves in the leftmost few strips *along* the direction of the strips. The resulting modulation of charge distribution in these strips capacitively couple to the neighboring strip to the right, exciting 2D plasmonic waves along the direction of the strip. This energy transfer process is repeated, delivering an *effective wave* from left to right, *perpendicularly* to 2DEG strips. Note that two types of waves are involved [Fig. 7(c)]; the 2D plasmonic wave traveling along each strip, and the effective wave propagating orthogonally to the strips. It is this effective wave that is negatively refracting.

Since no current passes across any strip center due to symmetry, only the lower half below the horizontal symmetry line, or half circuit, can be used in understanding the metamaterial. If we denote the voltage at the top end of the *m*-th half strip as $V_m(t)$, the effective wave can be represented by $\{V_1(t), V_2(t), V_3(t), \dots \}$ [Fig. 7(c)]. Each half strip may be modeled as a plasmonic transmission line supporting 2D plasmonic wave [Fig. 7(c)]. But as the plasmonic transmission line is short-circuit terminated to ground at its end and the plasmonic wavelength is much longer than the strip length in this design, the plasmonic transmission acts like a lumped 2D kinetic inductor, $L_k l$, where l is the effective length of the half strip. The entire half-circuit is then an array of capacitively coupled lumped kinetic inductors [Fig. 7(d)]. This may be likened to the left-handed electromagnetic transmission line, an array of capacitively coupled magnetic inductors, which is known to be negatively refracting [35,36]. However, with the significantly large 2D kinetic inductance, the 2DEG strip array yields a negative index as large as -700 [9], while the left-handed electromagnetic transmission line, which relies on 3~4 orders of magnitude smaller magnetic inductance, yields negative indices typically below -5.

We reviewed the unique characteristics of 2D plasmonic waves (in particular, their ultra-subwavelength confinement) and their underlying physics, and described how 2D plasmonic waves can be engineered by geometric shaping of 2D conductor to create 2D plasmonic circuits and metamaterials. The proof-of-concept devices presented were implemented with GaAs 2DEG, and operated at GHz frequencies, thus at cryogenic temperature. However, room temperature excitation of 2D plasmonic waves is possible at THz and infrared frequencies with both GaAs 2DEG and graphene [7,25], thus the demonstrated device designs can be scaled to these higher frequencies for room temperature operation.

Acknowledgements

References

1. Barnes WL, Dereux A, Ebbesen TW. 2003 Surface plasmon subwavelength optics. *Nature* **424**, 824-830. (doi:10.1038/nature01937)

2. Ebbesen TW, Lezec HJ, Ghaemi HF, Thio T, Wolff PA. 1998 Extraordinary optical transmission through sub-wavelength hole arrays. *Nature* **391**, 667-669. (doi:10.1038/35570)

3. Polman A. 2008 Plasmonics Applied. *Science* **322**, 868-869. (doi:10.1126/science.1163959)

4. Gramotnev DK, Bozhevolnyi SI. 2010 Plasmonics beyond the diffraction limit. *Nat. Photon.* **4**, 83–91. (doi:10.1038/nphoton.2009.282)

5. Stern F. 1967 Polarizability of a Two-Dimensional Electron Gas. *Phys. Rev. Lett.* **18**, 546-548. (doi:10.1103/PhysRevLett.18.546)

6. Andress WF, Yoon H, Yeung KYM, Qin L, West KW, Pfeiffer LN, Ham D. 2012 Ultra-subwavelength two-dimensional plasmonic circuits. *Nano Lett.* **12**, 2272-2277. (doi:10.1021/nl300046g)

7. Ju L, et al. 2011 Graphene plasmonics for tunable terahertz metamaterials. *Nature Nanotech.* **6**, 630-634. (doi:10.1038/nnano.2011.146)

8. Yeung KYM, Yoon H, Andress WF, West KW, Pfeiffer LN, Ham D. 2013 Two-path solid-state interferometry using ultra-subwavelength two-dimensional plasmonic waves. *Appl. Phys. Lett.* **102**, 021104. (doi:doi:10.1063/1.4775668)

9. Yoon H, Yeung KYM, Umansky V, Ham D. 2012 A Newtonian approach to extraordinarily strong negative refraction. *Nature* **488**, 65-69. (doi:10.1038/nature11297)

10. Luryi S. 1988 Quantum capacitance devices. *Appl. Phys. Lett.* **52**, 501–503. (doi:10.1063/1.99649)

11. Eguiluz A, Lee TK, Quinn JJ, Chiu KW. 1975 Interface excitations in metal-insulator-semiconductor structures. *Phys. Rev. B* **11**, 4989–4993. (doi:10.1103/PhysRevB.11.4989)

12. Xia J, Chen F, Li J, Tao N. 2009 Measurement of the quantum capacitance of graphene. *Nat. Nano.* **4**, 505-509. (doi:10.1038/nnano.2009.177)

13. Burke PJ, Spielman IB, Eisenstein JP, Pfeiffer LN, West KW. 2000 High frequency conductivity of the high-mobility two-dimensional electron gas. *Appl. Phys. Lett.* **76**, 745–747. (doi:10.1063/1.125881)

14. Novoselov KS, Geim AK, Morozov SV, Jiang D, Katsnelson MI, Grigorieva IV, Dubonos SV, Firsov AA. 2005 Two-dimensional gas of massless Dirac fermions in graphene. *Nature* **438**, 197-200. (doi:10.1038/nature04233)

15. Castro Neto AH, Guinea F, Peres NMR, Novoselov KS, Geim AK. 2009 The electronic properties of graphene. *Rev. Mod. Phys.* **81**, 109-162. (doi:10.1103/RevModPhys.81.109)

16. Chauhan J, Guo J. 2011 Assessment of high-frequency performance limits of graphene field-effect transistors. *Nano. Res.* **4**, 571–579. (doi:10.1007/s12274-011-0113-1)

17. Yoon H, Forsythe C, Wang L, Tombros N, Watanabe K, Taniguchi T, Hone J, Kim P, Ham D. 2013 Measurement of Collective Dynamical Mass of Dirac Fermions in Graphene. (currently under review)

18. Rana F. 2008 Graphene Terahertz Plasmon Oscillators. *IEEE Trans. Nanotechnol.***7**, 91–99. (doi:10.1109/TNANO.2007.910334)

19. Staffaroni M, Conway J, Vedantam S, Tang J, Yablonovitch E. 2012 Circuit analysis in metal-optics. *Phot. Nano. Fund. Appl.* **10**, 166–176. (doi:10.1016/j.photonics.2011.12.002)

20. Ehrenreich H, Cohen MH. 1959 Self-Consistent Field Approach to the Many-Electron Problem. *Phys. Rev.* **115**, 786-790. (doi:10.1103/PhysRev.115.786)

21. Hwang EH, Das Sarma S. 2007 Dielectric function, screening, and plasmons in two-dimensional graphene. *Phys. Rev. B* **75**, 205418. (doi:10.1103/PhysRevB.75.205418)

22. Ryzhii V, Satou A, Otsuji T. 2007 Plasma waves in two-dimensional electron-hole system in gated graphene heterostructures. *J. Appl. Phys.* **101**, 024509. (doi:10.1063/1.2426904)

23. Yan H, Li X, Chandra B, Tulevski G, Wu Y, Freitag M, Zhu W, Avouris P, Xia F. 2012 Tunable infrared plasmonic devices using graphene/insulator stacks. *Nat. Nanotechnol.* **7**, 330-334. (doi:10.1038/nnano.2012.59)

24. Chen J, et al. 2012 Optical nano-imaging of gate-tunable graphene plasmons. *Nature* advance online publication. (doi:10.1038/nature11254)

25. Meziani YM, Handa H, Knap W, Otsuji T, Sano E, Popov VV, Tsymbalov GM, Coquillat D, Teppe F. 2008 Room temperature terahertz emission from grating coupled two-dimensional plasmons. *Appl. Phys. Lett.* **92**, 201108. (doi:10.1063/1.2919097)

26. Yablonovitch E. 1987 Inhibited Spontaneous Emission in Solid-State Physics and Electronics. *Phys. Rev. Lett.* **58**, 2059–2062. (doi:10.1103/PhysRevLett.58.2059)

27. John S. 1987 Strong localization of photons in certain disordered dielectric superlattices. *Phys. Rev. Lett.* **58**, 2486-2489. (doi:10.1103/PhysRevLett.58.2486)

28. Pendry JB. 2000 Negative Refraction Makes a Perfect Lens. *Phys. Rev. Lett.* **85**, 3966. (doi:10.1103/PhysRevLett.85.3966)

29. Veselago VG. 1968 The Electrodynamics of Substances with Simultaneously Negative Values of ε and μ. *Sov. Phys. Uspekhi* **10**, 509-514. (doi:10.1070/PU1968v010n04ABEH003699)

30. Smith DR, Padilla WJ, Vier DC, Nemat-Nasser SC, Schultz S. 2000 Composite Medium with Simultaneously Negative Permeability and Permittivity. *Phys. Rev. Lett.* **84**, 4184-4187. (doi:10.1103/PhysRevLett.84.4184)

31. Shelby RA, Smith DR, Schultz S. 2001 Experimental Verification of a Negative Index of Refraction. *Science* **292**, 77-79. (doi:10.1126/science.1058847)

32. Pendry JB. 2004 A Chiral Route to Negative Refraction. *Science* **306**, 1353-1355. (doi: 10.1126/science.1104467)

33. Engheta N. 2007 Circuits with Light at Nanoscales: Optical Nanocircuits Inspired by Metamaterials. *Science* **317**, 1698-1702. (doi:10.1126/science.1133268)

34. Lezec HJ, Dionne JA, Atwater HA. 2007 Negative Refraction at Visible Frequencies. *Science* **316**, 430-432. (doi:10.1126/science.1139266)

35. Eleftheriades GV, Iyer AK, Kremer PC. 2002 Planar negative refractive index media using periodically L-C loaded transmission lines. *IEEE Trans. Microw. Theory Techn.* **50**, 2702-2712. (doi:10.1109/TMTT.2002.805197)

36. Grbic A, Eleftheriades GV. 2004 Overcoming the Diffraction Limit with a Planar Left-Handed Transmission-Line Lens. *Phys. Rev. Lett.* **92**, 117403. (doi:10.1103/PhysRevLett.92.117403)